Gold Nanoclusters-Doped With ^{64}Cu for CXCR4 Positron Emission Tomography Imaging of Breast Cancer and Metastasis

Yongfeng Zhao[†,§], **Lisa Detering**[†,§], **Deborah Sultan**[†], **Matthew L Cooper**[‡], **Meng You**[†], **Sangho Cho**[∥], **Stephanie L. Meier**[‡], **Hannah Luehmann**[†], **Guorong Sun**[∥], **Michael Rettig**[‡], **Farrokh Dehdashti**[†], **Karen L. Wooley**[∥], **John F. DiPersio**[‡], and **Yongjian Liu**[†,*]

[†]Mallinckrodt Institute of Radiology, Washington University, St. Louis, Missouri, 63110, United States

[‡]Department of Medicine, Washington University, St. Louis, Missouri, 63110, United States

[∥]Department of Chemistry, Department of Chemical Engineering, and Department of Materials Science and Engineering, Texas A&M University, College Station, TX 77842, United States

Abstract

As an emerging class of nanomaterial, nanoclusters hold great potential for biomedical applications due to their unique sizes and related properties. Herein, we prepared a ^{64}Cu doped gold nanoclusters ([64]CuAuNCs, hydrodynamic size: 4.2 ± 0.5 nm) functionalized with AMD3100 or (Plerixafor) for targeted positron emission tomography (PET) imaging of CXCR4, an up-regulated receptor on primary tumor and lung metastasis in a mouse 4T1 orthotopic breast cancer model. We prepared a targeted [64]CuAuNCs-AMD3100 (4.5 ± 0.4 nm) *via* one-step reaction with controlled conjugation of AMD3100 and specific activity, as well as improved colloid stability. *In vivo* pharmacokinetic evaluation showed favorable organ distribution and significant renal and fecal clearance within 48 h post injection. The expression of CXCR4 in tumors and metastasis was characterized by immunohistochemistry, western blot, and reverse transcription polymerase chain reaction analysis. PET imaging with [64]CuAuNCs-AMD3100 demonstrated sensitive and accurate detection of CXCR4 in engineered tumors expressing various levels of the receptor while competitive receptor blocking studies confirmed targeting specificity of the nanoclusters. In contrast to non-targeted [64]CuAuNCs and ^{64}Cu-AMD3100 alone, the targeted [64]CuAuNCs-AMD3100 detected up-regulated CXCR4 in early-stage tumors and pre-metastatic niche of lung earlier and with greater sensitivity. Taken together, we believe that [64]CuAuNCs-AMD3100 could serve as a useful platform for early and accurate detection of breast cancer and metastasis providing an essential tool to guide the treatment.

Graphical Abstract

Radioactive ^{64}Cu integrated gold nanoclusters were synthesized for CXCR4 targeted positron emission tomography imaging. The ultrasmall size of the nanoclusters enabled significant

---

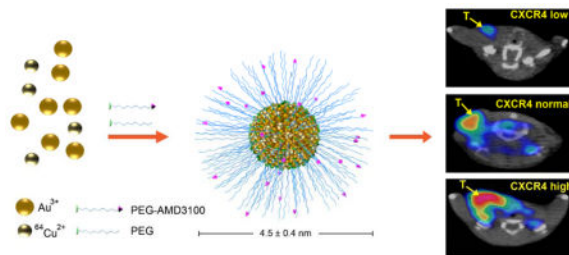[*]Corresponding Author: Address correspondence to: yongjianliu@wustl.edu.
[§]**Author Contributions**
These two authors contributed equally to this work.

clearance and low non-specific tumor retention. The superior pharmacokinetics and imaging accuracy demonstrated the potential of this CXCR4 targeted nanoclusters for translational research.

Keywords

CXCR4; nanocluster; breast cancer; lung metastasis; positron emission tomography

From the clinical viewpoint, the crucial step in breast cancer (BC) progression is the formation of metastases, which makes metastatic BC the second leading cause of cancer-related death among women.[1] Metastatic cancers are composed of heterogeneous cell populations with diverse metastatic potentials and organ specificity, indicating that the metastatic process is due, in part, to specific molecular characteristics of the metastasizing cells.[2] In BC, metastases can remain undetected for a long time after resection of the primary tumor as multiple secondary lesions can be triggered by yet unknown factors later.[3] The conventional pathological examination is limited, regarding sensitivity, accuracy, and reproducibility, due to the inadequate amount of tissue and heterogeneity of tumor. Thus, a sensitive and specific detection method targeting biomarkers up-regulated at primary tumors and metastatic organs at a molecular level would have a substantial clinical impact on the accurate determination of disease status and provide useful information to guide personalized treatment of patients.

Currently, most of the clinical imaging modalities for BC detection are largely anatomic in nature and lack both sensitivity and specificity to functionally detect BC invasion and metastasis, especially at distant sites, such as the lung.[4–6] Radionuclide-based molecular imaging techniques, such as positron emission tomography (PET), have been used to detect malignant cells within tumors and monitor treatment response, showing promise in assessing distant BC metastasis. However, the common clinical imaging agents, such as 2-deoxy-2-(^{18}F)fluoro-D-glucose (^{18}F-FDG), cannot target biomarkers specifically expressed on tumor cells and associated with tumor invasiveness and metastasis. Therefore, these generalized imaging agents lack the sensitivity and specificity to predict the risk of metastasis development in individual patients.[7, 8] As a result, a significant number of patients experience relapse in organs distant from primary tumors after the completion of therapy and ultimately die due to recurrence and metastasis.[3] There is an urgent need to develop non-invasive molecular imaging agents to sensitively and specifically detect the biomarkers expressed at metastatic sites, assess the connection between their up-regulation and metastasis, and prognostic potential to accurately predict the risk of metastasis development in individual patients.

Among the targets evaluated as prognostic markers for BC invasion and metastasis,[9–11] the chemokine receptor CXCR4 is of particular interest due to its interaction with the cognate ligand CXCL12, which is highly expressed at regional metastases to arrest the tumor cells expressing CXCR4 receptors.[12] Pre-clinical studies have shown a strong correlation between the overexpression of CXCR4 in primary tumors and the degree of regional metastases observed in BC.[13, 14] Clinically, the expression of CXCR4 was demonstrated to be critical for tumor proliferation, invasion, and the formation of metastases at distant sites in BC.[15] Further, by neutralizing the interaction of CXCL12/CXCR4, the metastasis of tumor cells to regional lymph nodes and the lung was significantly impaired,[16] indicating the potential of CXCR4 not only as a prognostic biomarker in promoting BC metastasis but also a target for therapy.[17]

Many molecular agents, including small molecules, peptides, proteins, and nanostructures, have been developed for CXCR4 imaging in various tumor models.[18–24] Most of them have focused on the detection of primary tumors, leaving their application for detection of distant metastasis underutilized. Further, the sensitivity of these agents in detecting the variation of CXCR4 in tumors has not been demonstrated.[24] Due to the less established vasculature and low expression of biomarkers at initial metastatic organs or the sites with potential for metastasis,[25] the imaging sensitivity and targeting specificity of these probes must be further improved to address the clinical challenge of defining metastatic potential.[26] Nanostructures, owing to their physicochemical properties, which afford enhanced sensitivity and specificity for early stage disease detection, have been widely used in oncological imaging.[27–31] However, the non-specific retention in tumors caused by enhanced permeability and retention (EPR) effect may hinder the understanding of imaging data and its correlation with the expression of prognostic biomarkers, confounding accurate tumor/metastasis grading. Herein, we report the preparation and application of a ultrasmall, renal clearable, CXCR4-targeted gold nanoclusters doped with the PET isotope ^{64}Cu and conjugated with a targeting ligand AMD3100, which is a CXCR4 antagonist approved for the mobilization of hematopoietic stem cells in lymphoma and multiple myeloma patients under the trademark Plerixafor (^{64}CuAuNCs-AMD3100) for tumor and lung metastasis detection in an orthotopic mouse 4T1 BC model.[32–40] The PET imaging sensitivity was demonstrated in CXCR4 knockdown and overexpression 4T1 models and the targeting specificity was confirmed through blocking studies. In contrast to the ligand tracer alone (^{64}Cu-AMD3100) and the non-targeted nanoclusters (^{64}CuAuNCs) without the conjugation of AMD3100, the targeted ^{64}CuAuNCs-AMD3100 demonstrated higher sensitivity, better accuracy and much earlier detection of CXCR4 expression in lung metastasis.

RESULTS AND DISCUSSION

Synthesis and characterization

It is known that gold nanostructure surface modification is driven by metal coordination (such as the Au-S bond) of the anchoring group onto the surface of the particle. The balance between the coordination number and surface grafting density is critical to the stability of nanostructures.[41] In this study, a bidentate thioctic acid-polyethylene glycol (TA-PEG) ligand was synthesized and utilized for surface modification of ^{64}CuAuNCs (Figure 1A,

Scheme S1), due to its high affinity and sulfur coverage for the Au surface, thus affording colloidal stability and low non-specific cellular binding for active targeting.[42–44] The preparation of targeted CuAuNCs-AMD3100 and non-targeted CuAuNCs was performed by following the procedure similar to that previously reported.[32] Typically, $CuCl_2$, $HAuCl_4$ and TA-PEG-AMD3100 or TA-PEG-OMe were mixed in water, followed by the addition of $NaBH_4$ solution under rapid stirring. The solution was then stirred at room temperature (RT) for 4 h prior to purification by centrifugal filtration. As shown in Figure 1B, transmission electron microscopy (TEM) showed that the as-prepared CuAuNCs-AMD3100 had uniform size distribution with a diameter of 1.7 ± 0.3 nm. Interestingly, in contrast to our previous report, the hydrodynamic sizes for both CuAuNCs-AMD3100 (4.5 ± 0.4 nm, Figure 1C and Table S1) and CuAuNCs (4.2 ± 0.5 nm) measured by dynamic light scattering (DLS) were slightly smaller than the CuAuNCs coated with monodentate PEG of the same molecular weight (750 Da, 5.6 ± 0.3 nm), presumably due to the constrained and compact structure of bidentate TA-PEG.[44] Consistent with other reports, there is no characteristic UV absorption between 550 nm and 600 nm for both nanoclusters, owing to their ultrasmall sizes (Figure S1A).[45] Following a previous report calculating the number of Au atoms in single nanocluster,[46] there were approximately 180 Au atoms in each as-prepared nanocluster, which accounted for ~ 40% of molecular weight of CuAuNCs (MW = 90 kDa) based on the thermogravimetric analysis. Thus, the number of PEG on CuAuNC was calculated as 60 copies/nanocluster. For the targeted nanocluster, since the molar ratio of TA-PEG-AMD3100 : TA-PEG-OMe was 1 : 2 in the reaction, there would be about 20 TA-PEG-AMD3100 and 40 TA-PEG-OMe on each CuAuNCs-AMD3100 with molecular weight around 100 kDa. The *in vitro* binding affinity of CuAuNCs-AMD3100 was measured and compared to AMD3100 ligand alone and non-targeted CuAuNCs.[22] As shown in Figure 1D, the targeted CuAuNCs-AMD3100 had slightly better binding affinity ($IC_{50}= 7.65$ nM) than AMD3100 ($IC_{50}= 10$ nM) in binding 12G5 domain while the non-targeted nanoclusters showed no binding. For the 1D9 control binding domain, neither CuAuNCs-AMD3100 nor AMD3100 showed binding (Figure S1C), indicating the binding specificity of targeted nanoclusters to CXCR4 receptor.[47]

The radiosyntheses of ^{64}CuAuNCs-AMD3100 and ^{64}CuAuNCs followed the same protocols as their non-radioactive counterparts with facilely controlled incorporation of ^{64}Cu by replacing $CuCl_2$ with $^{64}CuCl_2$, which enabled high radiolabeling specific activities (SA) for trace amount administration *in vivo* (^{64}CuAuNCs-AMD3100: SA= 192.4 MBq/nmol, injected dose= 19.2 pmol (1.92 μg)/mouse; ^{64}CuAuNCs: SA= 147.3 MBq/nmol, injected dose= 25.1 pmol (2.25 μg)/mouse), which were comparable to the mass of ^{64}CuAMD3100 used for PET (^{64}Cu-AMD3100: SA= 0.41 MBq/nmol, injected dose = 9.02 nmol (4.58 μg)/ mouse. Actually, these specific activities gave rise to one ^{64}Cu atom in every 8.50×10^3 and 1.11×10^4 Au atoms in ^{64}CuAuNCs-AMD3100 and ^{64}CuAuNCs, respectively, which was also consistent with the measurement of Cu: Au (1:500) ratio in non-radioactive CuAuNC acquired with inductively coupled plasma mass spectrometry given the fact that there were 10–20 non-radioactive carrier Cu atoms per ^{64}Cu atom.[48] Through straightforward centrifugal filtration, both nanoclusters could be quickly purified and available for pre-clinical PET imaging (Figure S1B). The *in vivo* radiolabel stability of ^{64}CuAuNCs was assessed by fast protein liquid chromatography analysis of serum samples separated from

blood collection at 1 h, 4 h and 24 h post injection. The radioactivity chromatograms showed 100% radiolabel stability up to 4 h and 92.5±1.2% (n=3) stability at 24 h, consistent with our previous report.[33]

In vivo pharmacokinetics and clearance

Due to their ultrasmall size, both [64]CuAuNCs-AMD3100 and [64]CuAuNCs showed rapid *in vivo* blood clearance ($t_{1/2}$ = 0.57 h and 1.22 h, respectively), which were consistent with the previously reported data.[49] *In vivo* pharmacokinetic evaluation showed that the overall blood pool (sum of blood, heart, and lung) retention of [64]CuAuNCs-AMD3100 was comparable to that obtained with non-targeted [64]CuAuNCs at each time point (Figure 2). The distribution profiles of the two nanoclusters in individual organs were similar except for the mononuclear phagocyte system (MPS) uptake. The liver and spleen accumulations of targeted [64]CuAuNCs-AMD3100 were significantly (p < 0.001, n = 4/group) higher than those acquired with [64]CuAuNCs at each time point during the 24 h study, which was likely due to the binding of [64]CuAuNCs-AMD3100 to CXCR4 receptors expressed on immune cells or inflammatory cells present in these two organs.[23, 24] Due to the high expression of CXCR4 in bone marrow,[38] the accumulation of [64]CuAuNCs-AMD3100 (7.09 ± 1.01 %ID/g) was twice as much as that of [64]CuAuNCs (3.05 ± 1.09 %ID/g, p < 0.001, n = 3/group) at 24 h post injection (p.i.). Interestingly, compared to the [64]CuAuNCs PEGylated with monothiol PEG350 (approximately 300 copies of PEG350),[32] the bidentate TA-PEG750 modified [64]CuAuNCs (approximately 60 copies) displayed similar systemic circulation while maintaining the identical hydrodynamic size, reasonably attributed to the enhanced stealth property provided by the relatively longer PEG chain length.

To translate inorganic nanostructures for clinical cancer imaging, renal excretion is a practical and effective strategy to facilitate this process.[30, 50] As revealed in Figure S2, the distinct sizes of both [64]CuAuNCs-AMD3100 and [64]CuAuNCs granted rapid and effective renal excretion (16.3 % and 27.0 % injected dose, respectively) at 4 h p.i.,[51] which showed increasing trend up to 24 h p.i. Besides rapid urinary excretion, both nanoclusters also showed slow but significant hepatobiliary clearance at 24 h (20.5 % and 26.4 % for [64]CuAuNCs-AMD3100 and [64]CuAuNCs, respectively).[32] It is noteworthy that the fecal clearance of [64]CuAuNCs-AMD3100 showed a further increase (18.8 % injected dose) at 48 h p.i., which was 6 times more than that acquired with [64]CuAuNCs at the same period and led to approximately 65% clearance of injected dose, similar to that of [64]CuAuNCs. This delayed clearance pattern was consistent with the decrease of liver uptake and elevated gastrointestinal tract (stomach and intestines) accumulation of [64]CuAuNCs-AMD3100 observed at 48 h p.i. Although the detailed mechanism is beyond the scope of this work, we hypothesize that the late fecal clearance of [64]CuAuNCs-AMD3100 is due to its binding to CXCR4 receptor expressed on various cells in the liver,[52] followed by receptor-mediated endocytosis and retention *in vivo*,[23] which consequently led to the postponed excretion through feces compared to the non-specific endocytosis of [64]CuAuNCs in hepatocytes.[32]

CXCR4 imaging sensitivity and specificity in primary tumors

To assess the sensitivity of targeted [64]CuAuNC detecting CXCR4, PET/CT imaging with [64]CuAuNCs-AMD3100 was performed in 4T1 tumor bearing mice implanted with

cells engineered with shRNAs expressing various levels of CXCR4 including knockdown, overexpression, and normal 4T1 cells with the presence of control shRNA (lacZ). As shown in figure 3A, when the CXCR4 RT-PCR analysis in normal 4T1 cells was set as 1, its relative expression in the CXCR4 knockdown, overexpression 4T1 cells and normal 4T1 cells with LacZ control shRNA were 0.47 ± 0.10, 1.73 ± 0.23, 1.02 ± 0.21 (n=3/group for all), respectively, confirming the effective engineering of CXCR4 expression in 4T1 cells. Consistent with the CXCR4 RT-PCR data acquired from the 4T1 cells, the RT-PCR data of total tumors displayed variable CXCR4 expression with relative ratios of 0.66 ± 0.10, 2.35 ± 0.25, 0.95 ± 0.21 in the knockdown, overexpression, and control LacZ shRNA groups (n=4/group for all) compared to the normal 4T1 tumor implanted with non-transfected cells (Figure 3B). Furthermore, the relative expressions of CXCR4 in the 4 types of tumors were similar to the variations of CXCR4 in the engineered cells, indicating the suitability of these models to assess the targeting specificity of developed nanoclusters.

Importantly, PET imaging with ^{64}CuAuNCs-AMD3100 demonstrated sensitive detection of CXCR4 in these 4T1 models expressing various levels of receptor at 1 week post implant (Figure 3C). The quantitative tumor uptake obtained at 24 h p.i. were 4.66 ± 0.62 %ID/g, 2.73 ± 0.16 %ID/g (p< 0.01, compared to normal 4T1 group), 6.67 ± 0.41 %ID/g (p< 0.05, compared to normal 4T1 group) (n=4/group for all) in the CXCR4 normal, knockdown, and overexpression groups, respectively (Figure 3D). The linear regression analysis showed a strong correlation between tumor CXCR4 levels and quantitative uptake (R^2=0.8998), confirming the sensitivity of ^{64}CuAuNCs-AMD3100 detecting CXCR4 in this tumor model. In the mice implanted with normal 4T1 cells transfected with control LacZ shRNA, the tumor uptake (5.07 ± 0.52 %ID/g, n=4/group) was similar (p> 0.05) to the data obtained in the normal 4T1 group, indicating the negligible effect of control shRNA on the tumor accumulation of targeted nanoclusters. Interestingly, with the dynamic release of AMD3100 (1.0 mg/day) from the Alzet pump as blocking agent for CXCR4, the tumor uptake of ^{64}CuAuNCs-AMD3100 was significantly blocked (3.19 ± 0.38 %ID/g, p< 0.05, n=4/group), confirming CXCR4 mediated tumor uptake. Additionally, the accumulations of ^{64}CuAuNCs-AMD3100 in these tumors normalized by tumor volumes (Table S2) also demonstrated correlation between CXCR4 RT-PCR data and total tumor uptake (R^2=0.9671), which further verified the specificity of this targeted nanocluster binding CXCR4 with minimal effect from tumor burden.

We next studied the targeting capability of ^{64}CuAuNCs-AMD3100 in mouse 4T1 tumor model and compared the imaging efficiency with ^{64}Cu-AMD3100 and non-targeted ^{64}CuAuNCs. As shown in Figure S3A, the bioluminescent images (BLI) of 4T1 tumor bearing mice at multiple time points post tumor implant displayed the aggressive progression of tumor mass over time with substantial necrosis observed in the tumor at day 28 post implant, which was also revealed by the histological analysis (Figure S4B). *Ex vivo* BLI of organs removed from the same animal showed significant metastasis in the lung, liver, and axillary lymph node and weak signals observed from bone, spleen, intestine, and brain (Figure S3B), in agreement with a previous report.[53] PET images of ^{64}Cu-AMD3100 clearly showed tracer accumulation (2.13 ± 0.17 %ID/g, n = 4/group) in the tumor at 1 week post tumor implant (Figure 4A, B). Additionally, the expression of CXCR4 was demonstrated *via* immunohistochemistry and western blot, as well as RT-PCR (Figures 5,

S5). Immunohistochemistry showed that most cells in the tumor and lung metastasis were positive for CXCR4 and the staining specificity was confirmed without using primary CXCR4 antibody showing no signal (Figure S5), which was further confirmed by western blot. RT-PCR of whole tumor demonstrated increased expression of CXCR4 during the 4 weeks. To normalize the interference of inflammatory cells expressing CXCR4 on the determination of elevated receptor concentration in lung due to metastasis, the RT-PCR data of CXCR4 in the lungs of tumor bearing mice was normalized by the results obtained from wild-type mice. As shown in Figure 5D, the increased ratios indicated the formation of metastasis in the lung with the progression of malignancy. With targeted ^{64}CuAuNCs-AMD3100, the tumor uptake was significantly improved to 7.15 ± 0.97 %ID/g, 2.4 times (p <0.0001, n = 4/group) higher than ^{64}Cu-AMD3100 and 1.3 times (p <0.05, n = 4/group) more than that obtained with control ^{64}CuAuNCs (3.08 ± 0.49 %ID/g), which was consistent with previous reports showing the low non-specific tumor retention of nanoclusters.[32] Thus, the ^{64}CuAuNCs-AMD3100 tumor uptake would be approximately 60% mediated by the CXCR4 binding. Importantly, the tumor-to-muscle ratio of ^{64}CuAuNCs-AMD3100 (18.9 ± 3.2, n = 4/group) was approximately 4 times higher than those obtained with either ^{64}Cu-AMD3100 (3.55 ± 0.68, p <0.0005, n = 4/group) or ^{64}CuAuNCs (3.79 ± 0.85, p <0.0005, n =4/group) (Figure 4C). Further, it was reported that the incorporation of metal ions into the cyclam rings of AMD3100 would significantly enhance the binding affinity to CXCR4.[54] However, the reducing agent of NaBH$_4$ employed in the synthesis of targeted nanoclusters reduced the metals including both ^{64}Cu^{2+} and Au^{3+} into elemental state, leading to little metal ions left in the solution for AMD3100 conjugation. This was confirmed by the gamma counting of filtrate after centrifugal purification of the nanoclusters showing little amount of radioactivity. Additionally, the ^{64}Cu radiolabeling of AMD3100 ligand alone in the presence of NaHB$_4$ showed little labeling, indicating the reduction of ^{64}Cu^{2+} into Cu atom which was unavailable for conjugation. Taken together, all these studies demonstrated the advantage of targeted nanoclusters for improved and more accurate detection of CXCR4 expression in tumor compared to the AMD3100 alone and non-targeted probe.

Of the imaging probes developed for CXCR4,[21, 22] the antagonist peptides and cyclam analogs have been widely studied in various mouse tumor models. In mouse 4T1 model, the^{111}In labeled TZ14011 tracer showed low tumor uptake (< 0.1%ID/g),[55] considerably lower than the results obtained with ^{64}CuAuNCs-AMD3100. In CXCR4 specifically transfected cell models, the T140 peptide based imaging agents and AMD3465 showed significant accumulation in primary tumor.[56–59] However, in other breast cancer models without specific CXCR4 transfection the uptake of these radiotracers were statistically lower that the data acquired in our 4T1 model using the targeted nanoclusters, which indicated the advantages of ^{64}CuAuNCs-AMD3100 for CXCR4 imaging including efficiency, sensitivity and specificity.

With progression of the 4T1 tumor and aggressive nature of the model, substantial tumor necrosis was observed in histological examination (Figure S4B), which might limit the delivery of nanoclusters for CXCR4 targeting as demonstrated by the heterogeneous distribution in tumors at 4 weeks post tumor implant (Figure 4A). More importantly, the necrosis also led to decreased CXCR4 receptor level expressed on 4T1 tumor cell surface after cell death due to the receptor degradation,[60, 61] which resulted in the decreased tumor

uptake of ^{64}CuAuNCs-AMD3100 (4.44 ± 0.64, n=4/group) at later time points (2, 3 and 4 weeks) post tumor implant (p < 0.01, n = 4/group) compared to the data obtained at week 1. However, due to the quickly expanded tumor volume demonstrated by BLI (Figure S3A) and tumor growth curve (Figure S4A), the rapidly proliferated tumor cells boosted the synthesis of CXCR4 RNA given the importance of this receptor in tumor growth,[62, 63] which was consistent with the increased RT-PCR data along the progression of the malignancy (Figure 5). Taken together, due to the limitation of ^{64}CuAuNCs-AMD3100 to track the progression of 4T1 tumor, it might be more useful as a targeted agent for early and sensitive detection of CXCR4 in tumor.

PET/CT imaging lung metastasis

Due to inadequately established vasculature and very low expression of biomarkers,[3] the early detection of cancer metastasis or imaging of metastatic potential continues to be a daunting task.[26, 64] According to figure S3C, tumor metastasis was identified in multiple organs including lung, liver spleen and intestines at week 4 using BLI. However, due to the significant non-specific accumulation or excretion, the localization of ^{64}CuAuNCs-AMD3100 in these organs did not show any difference during the 4 weeks' study. For example, histological analysis showed significant metastasis in liver at 4 weeks post tumor implant in contrast to normal liver H&E image without metastasis acquired at 2 weeks (Figure S6A). However, PET/CT imaging using ^{64}CuAuNCs-AMD3100 showed high liver accumulation and comparable uptake (20.3 ± 3.2%ID/g at 2 weeks vs. 24.6 ± 2.7 %ID/g at 4 weeks) at both time points in the 4T1 tumor bearing mice (Figure S6B), which was also similar to the data collected in the biodistribution studies using WT mice. Although the liver accumulations of ^{64}CuAuNCs-AMD3100 were at least 50% lower than the data acquired with other gold nanostructures with larger size (> 25 nm),[32, 65, 66] the high non-specific localization in liver due to the nature of nanoparticles prevented its application for liver metastasis detection.[67] Additionally, the size and surface charge of ^{64}CuAuNCs-AMD3100 might also limit its application in the diagnosis of brain metastasis. Thus, we had focused on the imaging of lung metastasis due to the low non-specific retention of targeted nanoclusters. As shown in figure 6A, ^{64}CuAuNCs-AMD3100 PET image showed specific accumulation in the lung (1.47 ± 0.22 %ID/g, n = 4/group) as early as 3 weeks post tumor implant, indicating the deposition of CXCR4 positive cells in the lung, while neither ^{64}Cu-AMD3100 (0.13 ± 0.03 %ID/g, p <0.0005, n = 4/group) nor ^{64}CuAuNCs (0.16 ± 0.03 %ID/g, p <0.0005, n = 4/group) showed any significant tracer accumulation in the lungs (Figure 6A, B). Also, histological examination of the lungs did not detect any metastasis (Figure S7). It indicated that the uptake of ^{64}CuAuNCs-AMD3100 in the lungs might be due to the binding to CXCR4 expressed by inflammatory cells but not tumor cells at pre-metastatic niche.[68, 69] This hypothesis was confirmed by the positive CD45 staining which served as an inflammatory biomarker in the lung and negative staining against green fluorescent protein (GFP) since the 4T1 tumor cells were transfected with GFP (Figure S8).[70] Additionally, *ex vivo* BLI at week 3 barely showed any signal in the lungs, confirming the binding of targeted nanocluster to pre-metastatic niche. At 4 weeks, H&E staining showed significant metastasis in lungs and RT-PCR demonstrated further elevated expression of CXCR4. Thus, the lung uptake of ^{64}CuAuNCs-AMD3100 in the same mice was further increased to 7.36 ± 0.03 %ID/g, more than 10 times higher than the results obtained with ^{64}Cu-AMD3100

(0.65 ± 0.16 %ID/g, p <0.0005, n=4/group). Interestingly, due to the ultrasmall size, only low non-specific retention was observed for ^{64}CuAuNCs (0.79 ± 0.13 %ID/g, p <0.0005, n = 4/group), indicating that the uptake of ^{64}CuAuNCs-AMD3100 was approximately 90% through CXCR4 receptor binding. The sensitive detection of CXCR4 at the metastatic lesion with targeted ^{64}CuAuNCs-AMD3100 led to high lung-to-muscle contrast ratios at 3 weeks (4.82 ± 0.61, n = 4/group) and 4 weeks (24.1 ± 5.69, n = 4/group) post tumor implant (Figure 6C), affording the capacity to detect BC metastatic potential. Additionally, PET images of ^{64}Cu-AMD3100 and ^{64}CuAuNCs-AMD3100 showed accumulation in spines (Figure 6A), reasonably due to the binding to the CXCR4 receptors expressed on hematopoietic cells in bone marrow, which was consistent with a previous report.[71] However, histological analysis did not detect any metastasis in the bone (Figure S9).

CONCLUSION

In summary, we have developed targeted ^{64}Cu doped gold nanoclusters with significant systemic clearance properties for accurate and sensitive detection of CXCR4 up-regulated in tumor and lung metastasis in a 4T1 mouse BC model. The flexible and straightforward preparation of ^{64}CuAuNCs-AMD3100 enabled high radiolabeling specific activity, thus creating sensitive PET probes for cancer imaging. The well-defined conjugation of the AMD3100 targeting ligand through a bidentate TA-PEG750 on ^{64}CuAuNCs-AMD3100 coupled with optimized pharmacokinetics afforded superior targeting capability in contrast to ^{64}Cu-AMD3100 alone and non-targeted ^{64}CuAuNCs. The low non-specific tumor retention, sensitive and specific detection of CXCR4 in the experimental mouse BC model demonstrates the advantages of targeted ^{64}CuAuNCs-AMD3100 to accurately determine the receptor in tumor and metastasis at early stage. However, its capability to determine tumor progression and burden needs further improvement. Taken together, this CXCR4 targeted nanoclusters showed potential in translational research for early cancer and metastasis diagnosis and may provide useful information to guide BC therapy *via* CXCR4 inhibition or chemotherapeutic agents.

MATERIALS AND METHODS

Chemicals

Amino-PEG 750 was purchased from BroadPharm (San Diego, U.S.A). All other chemicals were obtained from Sigma-Aldrich and used as received. Water with a resistivity of 18.2 MΩ cm was prepared using an E-Pure filtration system from Barnstead International (Dubuque, IA). ^{1}H NMR spectra were recorded either on a 300 MHz or 400 MHz NMR spectrometer (Varian/Agilent, Santa Clara, USA) maintained by the Washington University High Resolution NMR Facility.

Synthesis of TA-NHS (1)

Thioctic acid (0.41 g, 2 mmol) and *N*-hydroxysuccinimide (0.23 g, 2 mmol) were dissolved in dichloromethane (DCM) (4 mL) under argon atmosphere. After the solution was cooled to 0 °C, a solution of dicyclohexylcarbodiimide (DCC) (0.5 g, 2 mmol) in DCM (2 mL) was added. The mixture was stirred for 2 h, and then refrigerated overnight. The resulting

precipitate was filtered and the filtrate was dried under vacuum. The residue was washed with diethyl ether and dried under vacuum to get product **1** (0.54 g, 1.8 mmol, 89 % yield) as a pale yellow solid. ^{1}H NMR (CDCl$_3$, 400 MHz) δ (ppm): 3.56 (m, 1H, S-S-**CH$_2$**), 3.16 (m, 1H, S-S-**CH$_2$**), 3.10 (m, 1H, S-S-**CH**-), 2.82 (s, 4Hs, -CO**CH$_2$CH$_2$**CO-), 2.61 (t, 2Hs, J = 7.2 Hz, -**CH$_2$**CO-), 2.45 (sextet, 1H, J = 6.4 Hz, S-CH$_2$-**CH$_2$**-),1.92 (sextet, 1H, J =6.4 Hz, S-CH$_2$-**CH$_2$**-), 1.74 (m, 2Hs, -CH$_2$-**CH$_2$**-CO-)1.68 (m, 2Hs, -CH-**CH$_2$**-CH$_2$-), 1.55 (m, 2Hs, -CH-CH$_2$-**CH$_2$**-). ^{13}C NMR (CDCl$_3$, 1400 MHz) δ (ppm): 24.35, 25.57, 28.31, 30.77, 34.40, 38.51, 40.13, 56.07, 168.39, 169.09.

Synthesis of TA-PEG-COOH (2)

TA-NHS (0.045 g, 0.15 mmol) and NH$_2$-PEG750-COOH (0.10 g, 0.13 mmol) were dissolved in DCM (1 mL) under argon. Then triethylamine (50 μL) was added. After the solution was stirred overnight at RT, HCl (1M, 2 mL) was added to the solution. The mixture was extracted by DCM twice and the organic phases were combined and dried over anhydrous sodium sulfate. After evaporation of the solvent, the residue was purified by chromatography on silica gel (DCM : ethanol = 10 :2) to obtain the final product **2** (0.12 g, 0.12 mmol, 79 %) as a light yellow solid. ^{1}H NMR (CDCl$_3$, 400 MHz) δ (ppm): 6.23 (bs, 1H, -CO-**NH**-), 3.77 (t, 2Hs, J = 6.0 Hz, -**CH$_2$**-CH$_2$-CO), 3.65 (m, 52Hs, -O-**CH$_2$-CH$_2$**-O-), 3.56 (m, 1H, S-S-**CH$_2$**), 3.44 (m, 2Hs, -NH-CH$_2$-**CH$_2$**-O-), 3.16 (m, 1H, S-S-**CH$_2$**), 3.12 (m, 1H, S-S-**CH**-), 2.60 (t, 2Hs, J = 6.4 Hz, -**CH$_2$**CO-), 2.46 (sextet, 1H, J = 6.4 Hz, S-CH$_2$-**CH$_2$**-), 2.19 (t, 2Hs, J =7.6 Hz, -CH$_2$-**CH$_2$**-CO), 1.90 (sextet, 1H, J = 6.8 Hz, S-CH$_2$-**CH$_2$**-), 1.70 (m, 4Hs, -CH-**CH$_2$-CH$_2$**-), 1.45 (m, 2Hs, -NH-**CH$_2$**-). ^{13}C NMR (CDCl$_3$, 100 MHz) δ (ppm): 25.23, 28.74, 34.50, 34.77, 36.10, 38.31, 39.05, 40.07, 53.35, 56.27, 66.48, 69.73, 70.02, 70.17, 70.36, 172.95, 173.68.

Synthesis of TA-PEG-NHS (3)

TA-PEG-COOH (0.022 g, 0.022 mmol) and hydroxysuccinimide (0.0041g, 0.036 mmol) were dissolved in DCM (1 mL). After the solution was cooled to 0 °C, a solution of DCC (0.0065 g, 0.032 mmol) in DCM (0.5 mL) was slowly added to the solution. The mixture was stirred overnight. The resulting precipitate was filtered and the filtrate was evaporated under vacuum. The residue was washed with diethyl ether and dried under vacuum to get the product which was used directly for the next step without further purification.

Synthesis of TA-PEG-AMD3100 (4)

AMD3100 (0.040 g, 0.045 mmol) was dissolved in H$_2$O (0.9 mL), then NaHCO$_3$ (0.016 g, 0.19 mmol) was added to adjust the pH to 7–8. The solution of TA-PEG-NHS (0.024 g, 0.022 mmol) in tetrahydrofuran (THF) (1.4 mL) was added dropwise. After the mixture was stirred for two days at RT, the THF was evaporated. The resulting mixture was centrifuged and the supernatant was recovered. The aqueous phase was purified by RP-HPLC with H$_2$O/ acetonitrile solvent system to afford product **4** (0.0179g, 0.00959 mmol, 43% yield). MALDI-MS: calc'd. For C$_{71}$H$_{135}$N$_9$O$_{18}$S$_2$ (M)$^+$: 1465.94; found: 1465.60.

Synthesis of TA-PEG-OMe

To a mixture of thioctic acid (0.034 g, 0.17 mmol), DCC (0.035 g, 0.17 mmol) and 4-dimethylaminopyridine (0.0040 g, 0.033 mmol) in DCM (0.8 mL), a solution of NH_2-PEG750-OMe (0.13 g, 0.17 mmol) in DCM (0.4 mL) was added dropwise. After overnight stirring, the mixture was filtered, then rinsed with ethyl acetate. The combined filtrate was dried and the residue was dissolved in H_2O. The aqueous solution was extracted with diethyl ether once and saturated with $NaHCO_3$. The aqueous solution was extracted with DCM and the organic phase was dried over anhydrous sodium sulfate. After evaporation of the solvent, the residue was purified by chromatography on silica gel (DCM : ethanol = 10 :1, v/v) to obtain the final product as a light yellow solid. ^{1}H NMR ($CDCl_3$, 400 MHz) δ (ppm): 6.23 (bs, 1H), 3.64 (m), 3.53 (m, 4H), 3.43 (m, 2Hs), 3.37 (s, 3Hs), 3.16 (m, 1H), 3.12 (m, 1H), 2.46 (sextet, 1H, J = 6.4 Hz), 2.19 (t, 2Hs, J =7.6 Hz), 1.90 (m, 1H), 1.70 (m, 4Hs), 1.45 (m, 2Hs). ^{13}C NMR ($CDCl_3$, 100 MHz) δ (ppm): 25.37, 28.93, 34.66, 36.32, 38.45, 39.14, 40.22, 56.42, 59.04, 69.93, 70.20, 70.51, 70.55, 71.92, 172.77.

Synthesis of Non-radioactive CuAu Nanoclusters

In a typical reaction, water (0.488 mL), $HAuCl_4$ (10 mM, 50 μL), and $CuCl_2$ (1 mM, 5 μL) were mixed in a glass *via*l, followed by the dropwise addition of TA-PEG-OMe (MW=750Da, 2.5 mM, 600 μL). Sodium borohydride (40 mM, 175 μL) was added to the mixture with rapid stirring at RT and then continued for 4 hours. The CuAu nanoclusters (CuAuNCs) were purified by centrifugation filtration (Amicon, 10K) and washed with pH 7.4 phosphate buffer three times. To synthesize the targeted CuAuNC-AMD3100, TA-PEG-AMD3100 mixed with TA-PEG-OMe with 1:2 molar ratio was used for the synthesis following the same procedure.

Synthesis of ^{64}CuAuNCs and ^{64}CuAuNCs-AMD3100

The ^{64}Cu (half-life = 12.7 h, $β^+$ = 17%, $β^-$ = 40%) was produced at the Washington University cyclotron facility with specific activity of $518 ± 281$ GBq/μmol.[48, 72] ^{64}CuAuNCs and ^{64}CuAuNCs-AMD3100 were prepared following the same procedure as for non-radioactive CuAuNCs. For the targeted nanocluster, a mixture of TA-PEG-OMe (2.5 mM, 400 μL) and TA-PEG-AMD3100 (2.5 mM, 200 μL) with molar ratio of 2:1 was used for surface pegylation. Instead of adding $CuCl_2$, radioactive ^{64}CuCl$_2$ (157 MBq) was added. The synthesized ^{64}CuAuNCs and ^{64}CuAuNCs-AMD3100 was then purified by centrifugation filtration (Amicon, 10K) and washed with phosphate buffer (pH = 7.4) three times. The radiochemical purity was determined by spotting 1 μL of solution on instant thin layer chromatography paper (iTLC SG paper, Agilent Technology) and developed in glass TLC chamber with 10% ammonium acetate + methanol (1:1 volume ratio) mixture as developing solution for radioactive thin layer chromatography analysis (Radio-TLC, BioScan). When the radiochemical purity was equal or greater than 95%, the ^{64}CuAuNCs and ^{64}CuAuNCs-AMD3100 would be diluted in saline (3.7 MBq/100 μL) for intravenous injection through tail vein.

^{64}Cu radiolabeling of AMD3100

AMD3100 (120 μg, 0.24 μmol) was incubated with ^{64}Cu (100 MBq) in 50 μL of 0.1M NH_4OAc buffer (pH 5.5) at 60°C for 1 h with a yield of 97% according to Radio-TLC (BioScan). For PET imaging, 3.7 MBq ^{64}Cu-AMD3100 was diluted in 100 μL saline for intravenous injection through tail vein.

Characterizations of CuAuNCs and ^{64}CuAuNCs

The UV-Vis absorption spectra were recorded using a Cary 60 UV-Vis spectrometer (Agilent Technologies, Santa Clara, CA). The CuAuNCs were examined using a Tecnai G2 F20 ST transmission Electron Microscope (TEM) operated at 200 kV (FEI, Hillsboro, OR). Dynamic light scattering (NanoZS, Malvern, Worcestershire, UK) was performed to measure the hydrodynamic diameter and zeta-potential. The concentration of Au and Cu in the nanoclusters was measured by Elan DRC II inductively coupled plasma mass spectrometry (ICP-MS, Perkin-Elmer, Waltham, MA).

In vivo stability of ^{64}CuAuNCs

At 1 h, 4 h and 24 h post injection of 3.7 MBq ^{64}CuAuNCs through tail vein of Balb/c mice (n=3/time point), blood samples (100 μL) were collected into Vacutainer test tubes (BD, Franklin Lakes, NJ) and left in room temperature for 15 mins, followed by centrifugation at 1500 g for 15 min at 4 °C. The supernatant was diluted to 100 μL with PBS buffer (1X), added with ethylenediamine tetraacetic acid (5 μL, 10 mM in 50 mM pH 7 phosphate buffer), incubated at room temperature for 5 min, and injected into fast protein liquid chromatography (FPLC, ÄKTA, GE Healthcare). The FPLC system was equipped with a UV detector, a flow count radioactivity detector (Bioscan). The separation was accomplished with a superpose-12 10/300 size exclusion column (GE Healthcare) eluted with PBS (1X) buffer at a flow rate of 0.8 mL/min. The chromatograms were analyzed using UNICORN 4.1 software (GE Healthcare). The intact ^{64}CuAuNCs had a retention time of 10 ± 0.5 min and ^{64}Cu-EDTA came off the column at 17.4 ± 0.6 min. The serum samples were characterized by ^{64}CuAuNCs and ^{64}Cu-EDTA standards and the stability was calculated by the percent of radioactivity signal from ^{64}CuAuNCs in total radioactivity signals (sum of ^{64}CuAuNCs and ^{64}Cu-EDTA).

Characterization of density of PEG on the surface of Au Nanoclusters by thermogravimetric analysis (TGA)

In a typical measurement, about 2 mg dried AuNCs were heated on a TGA (TA instruments) from 30 °C to 600 °C at a rate of 10 °C/min under air atmosphere. The amount of TA-PEG conjugated onto the AuNCs was calculated based on the following equation:

$$N_{PEG} = \frac{A/M_{PEG}}{(1-A)/M_{Au}} \times N_{Au}$$

N_{PEG}: number of TA-PEG conjugated onto each AuNC

A: the percentage weight loss between 100 °C and 440 °C, which corresponds to the amount of TA-PEG on the surface

M_{PEG}: molecular weight of TA-PEG for the conjugation

M_{Au}: molecular weight of Au atom

N_{Au}: number of Au atom in each AuNC

Inhibition of anti-CXCR4 antibody binding to CXCR4

The CuAuNCs and CuAuNCs-AMD3100 were tested for CXCR4 specificity according to the following protocol. Human G2 acute lymphoblastic leukemia (ALL) cells which express CXCR4 were pre-incubated for 30 minutes at RT with vehicle control, 1 μM AMD3100 (positive control) or one of the as-prepared nanoclusters. Cells were then incubated with phycoerythrin-labeled anti-CXCR4 mAbs clone 12G5 or 1D9 or their corresponding isotype controls (muIgG2a or rtIgG2a) mAbs for 30 min at RT. Next, cells were washed in PBS containing 0.5% BSA and the %CXCR4+ cells was determined by flow cytometry. Since 12G5 binds to the SDF-1α site of CXCR4 where 1D9 does not, these data provide strong evidence that nanoparticles are specific CXCR4 binders to the SDF-1α binding site.

CXCR4 knockdown and overexpression in 4T1 cells

Control shRNA (LacZ) and shRNAs for murine CXCR4 in pLKO.1 lentiviral vectors were obtained from the Hope Center Viral Vectors Core at Washington University School of Medicine. Lentiviral particles were prepared with HEK-293T as the packaging cells according to the TRC (The RNAi Consortium) protocol. After infection of 4T1 cells with lentiviral particles, stable clones were selected in DMEM 10% FBS with 10 μg/mL puromycin (Invitrogen, San Diego, CA). To over express CXCR4, 4T1 cells were transfected with pcDNA3.1 (Invitrogen) containing murine CXCR4 cDNA (NM_009911.3) using FugeneHD transfection reagent (Promega, Madison, WI). Stably transfected clones were generated by culturing cells in 100 μg/ml G418 (Invitrogen) for 2 weeks. The expression of CXCR4 in the stably transfected cells were characterized by reverse transcription polymerase chain reaction (RTPCR) prior to tumor implant. The tumor sizes measured at 1 week post implant in the normal 4T1, LacZ shRNA, knockdown, and overexpression tumors were 122 ± 10 mm^3, 134 ± 15 mm^3, 65 ± 7 mm^3, and 243 ± 25 mm^3, respectively.

Bioluminescence imaging

At each time point after tumor implant, 4T1 tumor bearing mice were anesthetized with isoflurane and received an intraperitoneal injection of 200 μL luciferin solution (15 mg/mL) 10 min before bioluminescence and x-ray imaging using IVIS Lumina II XR System. Mice were scanned for 5 min and the images were analyzed using Living Image 3.0 software (Caliper life sciences, Hopkinton, MA). The optical signal was normalized to p/s/cm^2/Sr.

Animal Biodistribution Studies

All animal studies were performed in compliance with guidelines set forth by the NIH Office of Laboratory Animal Welfare and approved by the Washington University Animal Studies Committee. Normal female Balb/c mice (Charles River Laboratory, Wilmington, MA) were used for the biodistribution studies. About 370 kBq of ^{64}CuAuNCs or ^{64}CuAuNCs-AMD3100 in 100 μL saline (APP pharmaceuticals, Schaumburg, IL) was

injected *via* the tail vein. The mice were anesthetized with inhaled isoflurane and re-anesthetized before euthanasia by cervical dislocation at each time point (1 h, 4 h, and 24 h post injection, n = 4/group). Organs of interest were collected, weighed, and counted in a Beckman 8000 gamma counter (Beckman, Fullterton, CA). Standards were prepared and measured along with the samples to calculate percentage of the injected dose per gram of tissue (%ID/g). The mean blood half-lives of the two nanoclusters were calculated based on the blood retention data using a nonlinear regression analysis (Prism, version 6.04, Graphpad).

Clearance Studies

The clearance profile of ^{64}CuAuNCs and ^{64}CuAuNCs-AMD3100 was evaluated by measuring the radioactivity in urine and feces samples collected during the study. A group of mice (n = 4/group) were housed in a metabolism study cage where the urine and feces were separately collected at 4 h, 24 h, and 48 h post ^{64}CuAuNCs post ^{64}CuAuNCs-AMD3100 injection (370 kBq/animal). The gamma counting results were calculated as mean percentage of injected dose (%ID) for the group of mice.

Micro-PET/CT Imaging

The mouse 4T1 breast cancer cell lines (ATCC, Manassas, VA) transfected with GFP and luciferase were cultured in Dulbecco's Modified Eagle's Medium supplemented with 2 mM L-glutamine and 10% fetal bovine serum at 37 °C with 5% CO_2. Female balb/c mice at age 6 weeks (Charles River Laboratory, Wilmington, MA) were subcutaneously implanted with 3×10^5 4T1 cells into the mammary fat pad. The tumors were allowed to grow up to 4 weeks for the PET/CT imaging studies. For CXCR4 imaging sensitivity study, the tumor bearing mice implanted with 4T1 cells in the presence of control shRNA (LacZ), CXCR4 knockdown, CXCR4 overexpression, and non-transfected 4T1 cells were imaged at 1 week post-implant. Mice were anesthetized with isoflurane and injected with 3.7 MBq of ^{64}Cu-AMD3100, ^{64}CuAuNCs-AMD3100, and ^{64}CuAuNCs in 100 μL of saline *via* the tail vein. Small animal PET scans were performed on either microPET Focus 220 (Siemens, Malvern, PA) or Inveon PET/CT system (Siemens, Malvern, PA) at 1 hour (20 min frame), 4 hour (30 min frame), and 24 hour post-injection (60 min frame) for ^{64}CuAuNCs-AMD3100 and ^{64}CuAuNCs. For ^{64}Cu-AMD3100, a 0–60 min dynamic scan was performed. The microPET images were corrected for attenuation, scatter, normalization, and camera dead time and co-registered with microCT images. All of the PET scanners were cross-calibrated periodically. The microPET images were reconstructed with the maximum a posteriori (MAP) algorithm and analyzed by Inveon Research Workplace. The tumor uptake was calculated in terms of the percent injected dose per gram (%ID/g) of tumor tissue in three-dimensional regions of interest (ROIs) without the correction for partial volume effect.

The competitive PET blocking study was done by AMD3100 suspended in PBS and filled into Alzet osmotic minipumps (model 2001, 1.0 μL/h, Alzet, Palo Alto, CA) to continuously release 1 mg AMD3100/day. Osmotic minipumps were sterilely implanted into a subcutaneous pouch in the back under general anesthesia as described at 24 h prior to the PET imaging.[73]

Histopathology and immunohistochemistry

Tumor and lung serial sections (5-μm thick) were cut from paraformaldehyde-fixed (24 h), paraffin-embedded specimens. The sections were deparaffinized and stained with hematoxylin and eosin. For immunohistochemistry, the sections were deparaffinized and rehydrated through a series of xylenes and graded alcohols before undergoing antigen retrieval pretreatment (10 mM Tris, 1 mM ethylenediaminetetraacetic acid, 0.05% polysorbate, pH 9.0, for 10 min). They were incubated in blocking serum for 1 h to prevent nonspecific binding (Vectastain; Vector Laboratories). The sections were then incubated overnight at 4 °C with primary antibody (anti-CXCR4, 1:200 in blocking serum; Abcam). Secondary antibody was applied (Vector Laboratories), and color development was activated by alkaline phosphatase to give an intense blue color. The sections were counterstained with nuclear fast red to reveal the tissue architecture (pink). Digital images of the stained sections were obtained using a scanning light microscope (NanoZoomer; Hamamatsu).

CD45 and green fluorescent protein (GFP) staining was performed using a similar protocol. Briefly, after serum blocking, mouse lung sections were incubated for one hour at room temperature with primary antibody (anti-CD45, 1:250 in blocking serum, BD Biosciences, San Jose, CA or anti-GFP, 1:500 in blocking serum, Biolegend, San Diego, CA). Secondary antibody was applied (Vector Laboratories) and color development was achieved through diaminobenzidine (DAB)-based immunostaining kits (Vector Laboratories). Sections were counterstained with hematoxylin. Digital images of the stained sections were obtained using a light microscope (Leica). Hematoxylin and eosin (H&E) was performed on consecutively cut sections for morphological characterization of the tissue.

RT-PCR

RNA isolated from 4T1 primary tumor and lungs were used for real time RT-PCR. Tissue RNA was isolated using TRIzol (Invitrogen) per the manufacturer's instruction. Reverse transcription reactions used 1 μg of total RNA, random hexamer priming, and Superscript II reverse transcriptase (Invitrogen). Expression of CXCR4 and β-actin were determined using Taqman assays (Invitrogen) and an EcoTM Real-Time PCR System (Illumina) in duplicate in 48-well plates. PCR cycling conditions were as follows: 50 °C for 2 min, 95 °C for 21 sec and 60 °C for 20 sec. β-actin expression was used as a comparator using $\Delta\Delta C_t$ calculations.

Western blot

Frozen 4T1 tumors and organ tissues were homogenized in NP40 buffer (50 mM Tris pH 8.0, 150 mM NaCl, 1% NP-40) supplemented with protease inhibitor cocktail (Sigma-Aldrich, St. Louis, MO). The lysates were centrifuged at 4 °C and the supernatants were collected as the protein extracts. The protein content of each sample was determined using the Bio-rad protein assay (Bio-rad, Hercules, CA). Eighty μg of total protein from each sample were separated on a 12% SDS-PAGE and then electrophoretically transferred onto nitrocellulose membrane (Bio-rad, Hercules, CA). The membranes were blocked in PBS-T (0.1% Tween-20) containing 5% non-fat milk powder for 1 h to inhibit non-specific binding, and then incubated with rabbit anti-CXCR4 antibodies (dilution 1:1000, ab2074, Abcam, Cambridge, MA) overnight at 4 °C. After washing with PBS-T, the membranes were incubated with horseradish peroxidase-linked antirabbit IgG (dilution 1:5000; GE

Healthcare Bio-Sciences, Pittsburgh, PA) for 45 min at RT, followed by chemiluminescent detection with ECL substrate (GE Healthcare Bio-Sciences, Pittsburgh, PA) for 1 min. The images were exposed and captured immediately. For normalization, β-actin was detected as internal standard in parallel blots.

Statistical analysis

Group variation is described as mean ± SD. Groups were compared using 1-way ANOVA with a Bonferroni posttest. Individual group differences were determined with use of a 2-tailed Mann–Whitney test. The significance level in all tests was P ≤0.05. Prism, version 6.04 (Graphpad), was used for all statistical analyses.

Supplementary Material

Refer to Web version on PubMed Central for supplementary material.

Acknowledgments

References

1. Weigelt B, Peterse JL, van 't Veer LJ. Breast Cancer Metastasis: Markers and Models. Nat Rev Cancer. 2005; 5:591–602. [PubMed: 16056258]

2. Lorusso G, Ruegg C. nov Insights into the Mechanisms of Organ-Specific Breast Cancer Metastasis. Semin Cancer Biol. 2012; 22:226–233. [PubMed: 22504658]

3. Scully OJ, Bay BH, Yip G, Yu Y. Breast Cancer Metastasis. Cancer Genomics Proteomics. 2012; 9:311–320. [PubMed: 22990110]

4. Iima M, Kataoka M, Okumura R, Togashi K. Detection of Axillary Lymph Node Metastasis with Diffusion-Weighted MR Imaging. Clin Imaging. 2014; 38:633–636. [PubMed: 24908365]

5. Warner E, Plewes DB, Shumak RS, Catzavelos GC, Di Prospero LS, Yaffe MJ, Goel V, Ramsay E, Chart PL, Cole DE, Taylor GA, Cutrara M, Samuels TH, Murphy JP, Murphy JM, Narod SA. Comparison of Breast Magnetic Resonance Imaging, Mammography, and Ultrasound for Surveillance of Women at High Risk for Hereditary Breast Cancer. J Clin Oncol. 2001; 19:3524–3531. [PubMed: 11481359]

6. Kuhl CK, Schrading S, Leutner CC, Morakkabati-Spitz N, Wardelmann E, Fimmers R, Kuhn W, Schild HH. Mammography, Breast Ultrasound, and Magnetic Resonance Imaging for Surveillance of Women at High Familial Risk for Breast Cancer. J Clin Oncol. 2005; 23:8469–8476. [PubMed: 16293877]

7. Mankoff DA, Specht JM, Eubank WB, Kessler L. [(18)F]Fluorodeoxyglucose Positron Emission Tomography-Computed Tomography in Breast Cancer: When... And When Not? J Clin Oncol. 2012; 30:1252–1254. [PubMed: 22393078]

8. Specht JM, Mankoff DA. Advances in Molecular Imaging for Breast Cancer Detection and Characterization. Breast Cancer Res. 2012; 14:206. [PubMed: 22423895]

9. Wang Q, Diao X, Sun J, Chen Z. Regulation of Vegf, Mmp-9 and Metastasis by CXCR4 in a Prostate Cancer Cell Line. Cell Biol Int. 2011; 35:897–904. [PubMed: 21306303]

10. Banin Hirata BK, Oda JM, Losi Guembarovski R, Ariza CB, de Oliveira CE, Watanabe MA. Molecular Markers for Breast Cancer: Prediction on Tumor Behavior. Dis Markers. 2014; 2014:513158. [PubMed: 24591761]

11. Trop I, LeBlanc SM, David J, Lalonde L, Tran-Thanh D, Labelle M, El Khoury MM. Molecular Classification of Infiltrating Breast Cancer: Toward Personalized Therapy. Radiographics. 2014; 34:1178–1195. [PubMed: 25208275]

12. Muller A, Homey B, Soto H, Ge N, Catron D, Buchanan ME, McClanahan T, Murphy E, Yuan W, Wagner SN, Barrera JL, Mohar A, Verastegui E, Zlotnik A. Involvement of Chemokine Receptors in Breast Cancer Metastasis. Nature. 2001; 410:50–56. [PubMed: 11242036]

13. Kang H, Watkins G, Douglas-Jones A, Mansel RE, Jiang WG. The Elevated Level of CXCR4 Is Correlated with Nodal Metastasis of Human Breast Cancer. Breast. 2005; 14:360–367. [PubMed: 16216737]

14. Woo SU, Bae JW, Kim CH, Lee JB, Koo BW. A Significant Correlation between Nuclear Cxcr4 Expression and Axillary Lymph Node Metastasis in Hormonal Receptor Negative Breast Cancer. Ann Surg Oncol. 2008; 15:281–285. [PubMed: 17763975]

15. Salvucci O, Bouchard A, Baccarelli A, Deschenes J, Sauter G, Simon R, Bianchi R, Basik M. The Role of CXCR4 Receptor Expression in Breast Cancer: A Large Tissue Microarray Study. Breast Cancer Res Treat. 2006; 97:275–283. [PubMed: 16344916]

16. Gil M, Seshadri M, Komorowski MP, Abrams SI, Kozbor D. Targeting CXCL12/CXCR4 Signaling with Oncolytic Virotherapy Disrupts Tumor Vasculature and Inhibits Breast Cancer Metastases. Proc Natl Acad Sci US A. 2013; 110:E1291–1300.

17. Papatheodorou H, Papanastasiou AD, Sirinian C, Scopa C, Kalofonos HP, Leotsinidis M, Papadaki H. Expression Patterns of SDF1/CXCR4 in Human Invasive Breast Carcinoma and Adjacent Normal Stroma: Correlation with Tumor Clinicopathological Parameters and Patient Survival. Pathol Res Pract. 2014; 210:662–667. [PubMed: 25041836]

18. Zhang XX, Sun Z, Guo J, Wang Z, Wu C, Niu G, Ma Y, Kiesewetter DO, Chen X. Comparison of (18)F-Labeled CXCR4 Antagonist Peptides for PET Imaging of CXCR4 Expression. Mol Imaging Biol. 2013; 15:758–767. [PubMed: 23636490]

19. Woodard LE, De Silva RA, Behnam Azad B, Lisok A, Pullambhatla M, WGL, Mease RC, Pomper MG, Nimmagadda S. Bridged Cyclams as Imaging Agents for Chemokine Receptor 4 (CXCR4). Nucl Med Biol. 2014; 41:552–561. [PubMed: 25038987]

20. Hartimath SV, van Waarde A, Dierckx RA, de Vries EF. Evaluation of N-[C]Methyl-AMD3465 as a PET Tracer for Imaging of CXCR4 Receptor Expression in a C6 Glioma Tumor Model. Mol Pharm. 2014; 11:3810–1817. [PubMed: 25094028]

21. Weiss ID, Jacobson O. Molecular Imaging of Chemokine Receptor CXCR4. Theranostics. 2013; 3:76–84. [PubMed: 23382787]

22. Kuil J, Buckle T, van Leeuwen FW. Imaging Agents for the Chemokine Receptor 4 (CXCR4). Chem Soc Rev. 2012; 41:5239–5261. [PubMed: 22743644]

23. De Silva RA, Peyre K, Pullambhatla M, Fox JJ, Pomper MG, Nimmagadda S. Imaging CXCR4 Expression in Human Cancer Xenografts: Evaluation of Monocyclam 64Cu-AMD3465. J Nucl Med. 2011; 52:986–993. [PubMed: 21622896]

24. Nimmagadda S, Pullambhatla M, Stone K, Green G, Bhujwalla ZM, Pomper MG. Molecular Imaging of CXCR4 Receptor Expression in Human Cancer Xenografts with [64Cu]AMD3100 Positron Emission Tomography. Cancer Res. 2010; 70:3935–3944. [PubMed: 20460522]

25. Murphy EA, Majeti BK, Barnes LA, Makale M, Weis SM, Lutu-Fuga K, Wrasidlo W, Cheresh DA. Nanoparticle-Mediated Drug Delivery to Tumor Vasculature Suppresses Metastasis. Proc Natl Acad Sci US A. 2008; 105:9343–9348.

26. Winnard PT Jr, Pathak AP, Dhara S, Cho SY, Raman V, Pomper MG. Molecular Imaging of Metastatic Potential. J Nucl Med. 2008; 49(Suppl 2):96S–112S. [PubMed: 18523068]

27. Pressly ED, Pierce RA, Connal LA, Hawker CJ, Liu Y. Nanoparticle PET/CT Imaging of Natriuretic Peptide Clearance Receptor in Prostate Cancer. Bioconjug Chem. 2013; 24:196–204. [PubMed: 23272904]

28. Guo Y, Aweda T, Black KC, Liu Y. Chemistry and Theranostic Applications of Radiolabeled Nanoparticles for Cardiovascular, Oncological, and Pulmonary Research. Curr Top Med Chem. 2013; 13:470–478. [PubMed: 23432009]

29. Liu Y, Welch MJ. Nanoparticles Labeled with Positron Emitting Nuclides: Advantages, Methods, and Applications. Bioconjug Chem. 2012; 23:671–682. [PubMed: 22242601]

30. Chow EK, Ho D. Cancer Nanomedicine: From Drug Delivery to Imaging. Sci Transl Med. 2013; 5:216rv214.

31. Ferrari M. Cancer Nanotechnology: Opportunities and Challenges. Nat Rev Cancer. 2005; 5:161–171. [PubMed: 15738981]

32. Zhao Y, Sultan D, Detering L, Luehmann H, Liu Y. Facile Synthesis, Pharmacokinetic and Systemic Clearance Evaluation, and Positron Emission Tomography Cancer Imaging of 64Cu-Au Alloy Nanoclusters. Nanoscale. 2014; 6:13501–13509. [PubMed: 25266128]

33. Zhao Y, Sultan D, Detering L, Cho S, Sun G, Pierce R, Wooley KL, Liu Y. Copper-64-Alloyed Gold Nanoparticles for Cancer Imaging: Improved Radiolabel Stability and Diagnostic Accuracy. Angew Chem Int Ed Engl. 2014; 53:156–159. [PubMed: 24272951]

34. Liu J, Yu M, Zhou C, Yang S, Ning X, Zheng J. Passive Tumor Targeting of Renal-Clearable Luminescent Gold Nanoparticles: Long Tumor Retention and Fast Normal Tissue Clearance. J Am Chem Soc. 2013; 135:4978–4981. [PubMed: 23506476]

35. Liu J, Yu M, Zhou C, Zheng J. Renal Clearable Inorganic Nanoparticles: A New Frontier of Bionanotechnology. Mater Today. 2013; 16:477–486.

36. Cashen AF, Nervi B, DiPersio J. AMD3100: CXCR4 Antagonist and Rapid Stem Cell-Mobilizing Agent. Future Oncol. 2007; 3:19–27. [PubMed: 17280498]

37. DiPersio JF, Uy GL, Yasothan U, Kirkpatrick P. Plerixafor. Nat Rev Drug Discov. 2009; 8:105–106. [PubMed: 19180104]

38. Rettig MP, Ramirez P, Nervi B, DiPersio JF. CXCR4 and Mobilization of Hematopoietic Precursors. Methods Enzymol. 2009; 460:57–90. [PubMed: 19446720]

39. Gravekamp C, Leal B, Denny A, Bahar R, Lampkin S, Castro F, Kim SH, Moore D, Reddick R. *In vivo* Responses to Vaccination with Mage-B, Gm-Csf and Thioglycollate in a Highly Metastatic Mouse Breast Tumor Model, 4T1. Cancer Immunol Immunother. 2008; 57:1067–1077. [PubMed: 18094967]

40. Pulaski BA, Ostrand-Rosenberg S. Mouse 4T1 Breast Tumor Model. Curr Protoc Immunol. 2001; Chapter 20(Unit 20):22.

41. Mei BC, Oh E, Susumu K, Farrell D, Mountziaris TJ, Mattoussi H. Effects of Ligand Coordination Number and Surface Curvature on the Stability of Gold Nanoparticles in Aqueous Solutions. Langmuir. 2009; 25:10604–10611. [PubMed: 19588955]

42. Oh E, Susumu K, Jain V, Kim M, Huston A. One-Pot Aqueous Phase Growth of Biocompatible 15–130 nm Gold Nanoparticles Stabilized with Bidentate PEG. J Colloid Interface Sci. 2012; 376:107–111. [PubMed: 22480398]

43. Oh E, Delehanty JB, Sapsford KE, Susumu K, Goswami R, Blanco-Canosa JB, Dawson PE, Granek J, Shoff M, Zhang Q, Goering PL, Huston A, Medintz IL. Cellular Uptake and Fate of Pegylated Gold Nanoparticles Is Dependent on Both Cell-Penetration Peptides and Particle Size. ACS Nano. 2011; 5:6434–6448. [PubMed: 21774456]

44. Oh E, Susumu K, Makinen AJ, Deschamps JR, Huston AL, Medintz IL. Colloidal Stability of Gold Nanoparticles Coated with Multithiol-Poly(Ethylene Glycol) Ligands: Importance of Structural Constraints of the Sulfur Anchoring Groups. J Phys Chem C. 2013; 117:18947–18956.

45. Zhang XD, Wu D, Shen X, Liu PX, Fan FY, Fan SJ. *In vivo* Renal Clearance, Biodistribution, Toxicity of Gold Nanoclusters. Biomaterials. 2012; 33:4628–4638. [PubMed: 22459191]

46. Wuelfing WP, Gross SM, Miles DT, Murray RW. Nanometer Gold Clusters Protected by Surface-Bound Monolayers of Thiolated Poly(Ethylene Glycol) Polymer Electrolyte. J Am Chem Soc. 1998; 120:12696–12697.

47. Donzella GA, Schols D, Lin SW, Este JA, Nagashima KA, Maddon PJ, Allaway GP, Sakmar TP, Henson G, De Clercq E, Moore JP. Amd3100, a Small Molecule Inhibitor of HIV-1 Entry *via* the CXCR4 Co-Receptor. Nat Med. 1998; 4:72–77. [PubMed: 9427609]

48. Kume M, Carey PC, Gaehle G, Madrid E, Voller T, Margenau W, Welch MJ, Lapi SE. A Semi-Automated System for the Routine Production of Copper-64. Appl Radiat Isot. 2012; 70:1803–1806. [PubMed: 22516717]

49. Liu J, Yu M, Ning X, Zhou C, Yang S, Zheng J. Pegylation and Zwitterionization: Pros and Cons in the Renal Clearance and Tumor Targeting of Near-IR-Emitting Gold Nanoparticles. Angew Chem Int Ed Engl. 2013; 52:12572–12576. [PubMed: 24123783]

50. Phillips E, Penate-Medina O, Zanzonico PB, Carvajal RD, Mohan P, Ye Y, Humm J, Gonen M, Kalaigian H, Schoder H, Strauss HW, Larson SM, Wiesner U, Bradbury MS. Clinical Translation of an Ultrasmall Inorganic Optical-PET Imaging Nanoparticle Probe. Sci Transl Med. 2014; 6:260ra149.

51. Almeida JP, Chen AL, Foster A, Drezek R. *In vivo* Biodistribution of Nanoparticles. Nanomedicine. 2011; 6:815–835. [PubMed: 21793674]

52. Shibuta K, Mori M, Shimoda K, Inoue H, Mitra P, Barnard GF. Regional Expression of CXCL12/CXCR4 in Liver and Hepatocellular Carcinoma and Cell-Cycle Variation During *In Vitro* Differentiation. Jpn J Cancer Res. 2002; 93:789–797. [PubMed: 12149145]

53. Smith MC, Luker KE, Garbow JR, Prior JL, Jackson E, Piwnica-Worms D, Luker GD. CXCR4 Regulates Growth of Both Primary and Metastatic Breast Cancer. Cancer Res. 2004; 64:8604–8612. [PubMed: 15574767]

54. Gerlach LO, Jakobsen JS, Jensen KP, Rosenkilde MR, Skerlj RT, Ryde U, Bridger GJ, Schwartz TW. Metal Ion Enhanced Binding of AMD3100 to ASP262 in the CXCR4 Receptor. Biochemistry. 2003; 42:710–717. [PubMed: 12534283]

55. Buckle T, Kuil J, van den Berg NS, Bunschoten A, Lamb HJ, Yuan H, Josephson L, Jonkers J, Borowsky AD, van Leeuwen FW. Use of a Single Hybrid Imaging Agent for Integration of Target Validation with *in vivo* and *ex vivo* Imaging of Mouse Tumor Lesions Resembling Human Dcis. PLoS One. 2013; 8:e48324. [PubMed: 23326303]

56. De Silva RA, Peyre K, Pullambhatla M, Fox JJ, Pomper MG, Nimmagadda S. Imaging CXCR4 Expression in Human Cancer Xenografts: Evaluation of Monocyclam 64Cu-AMD3465. J Nucl Med. 2011; 52:986–993. [PubMed: 21622896]

57. Hartimath SV, van Waarde A, Dierckx RA, de Vries EF. Evaluation of N-[(11)C]Methyl-AMD3465 as a PET Tracer for Imaging of CXCR4 Receptor Expression in a C6 Glioma Tumor Model. Mol Pharm. 2014; 11:3810–3817. [PubMed: 25094028]

58. Jacobson O, Weiss ID, Szajek LP, Niu G, Ma Y, Kiesewetter DO, Peled A, Eden HS, Farber JM, Chen X. Improvement of CXCR4 Tracer Specificity for PET Imaging. J Control Release. 2012; 157:216–223. [PubMed: 21964282]

59. Yan X, Niu G, Wang Z, Yang X, Kiesewetter DO, Jacobson O, Shen B, Chen X. Al[(18)F]NOTA-T140 Peptide for Noninvasive Visualization of CXCR4 Expression. Mol Imaging Biol. 2016; 18:135–142. [PubMed: 26126597]

60. Hochreiter-Hufford A, Ravichandran KS. Clearing the Dead: Apoptotic Cell Sensing, Recognition, Engulfment, and Digestion. Cold Spring Harb Perspect Biol. 2013; 5:a008748. [PubMed: 23284042]

61. He B, Lu N, Zhou Z. Cellular and Nuclear Degradation During Apoptosis. Curr Opin Cell Biol. 2009; 21:900–912. [PubMed: 19781927]

62. Luker KE, Luker GD. Functions of CXCL12 and CXCR4 in Breast Cancer. Cancer Lett. 2006; 238:30–41. [PubMed: 16046252]

63. Chatterjee S, Behnam Azad B, Nimmagadda S. The Intricate Role of CXCR4 in Cancer. Adv Cancer Res. 2014; 124:31–82. [PubMed: 25287686]

64. Zhang Y, Hong H, Nayak TR, Valdovinos HF, Myklejord DV, Theuer CP, Barnhart TE, Cai W. Imaging Tumor Angiogenesis in Breast Cancer Experimental Lung Metastasis with Positron Emission Tomography, Near-Infrared Fluorescence, and Bioluminescence. Angiogenesis. 2013; 16:663–674. [PubMed: 23471463]

65. Wang Y, Liu Y, Luehmann H, Xia X, Wan D, Cutler C, Xia Y. Radioluminescent Gold Nanocages with Controlled Radioactivity for Real-Time *In Vivo* Imaging. Nano Lett. 2013; 13:581–585. [PubMed: 23360442]

66. Pang B, Zhao Y, Luehmann H, Yang X, Detering L, You M, Zhang C, Zhang L, Li ZY, Ren Q, Liu Y, Xia Y. (64)Cu-Doped Pdcu@Au Tripods: A Multifunctional Nanomaterial for Positron Emission Tomography and Image-Guided Photothermal Cancer Treatment. ACS Nano. 2016; 10:3121–3131. [PubMed: 26824412]

67. Moghimi SM, Hunter AC, Murray JC. Long-Circulating and Target-Specific Nanoparticles: Theory to Practice. Pharmacol Rev. 2001; 53:283–318. [PubMed: 11356986]

68. Sarchio SN, Scolyer RA, Beaugie C, McDonald D, Marsh-Wakefield F, Halliday GM, Byrne SN. Pharmacologically Antagonizing the CXCR4-CXCL12 Chemokine Pathway with AMD3100 Inhibits Sunlight-Induced Skin Cancer. J Invest Dermatol. 2014; 134:1091–1100. [PubMed: 24226205]

69. Ogawa F, Amano H, Eshima K, Ito Y, Matsui Y, Hosono K, Kitasato H, Iyoda A, Iwabuchi K, Kumagai Y, Satoh Y, Narumiya S, Majima M. Prostanoid Induces Premetastatic Niche in Regional Lymph Nodes. J Clin Invest. 2014; 124:4882–4894. [PubMed: 25271626]

70. Zaslona Z, Przybranowski S, Wilke C, van Rooijen N, Teitz-Tennenbaum S, Osterholzer JJ, Wilkinson JE, Moore BB, Peters-Golden M. Resident Alveolar Macrophages Suppress, Whereas Recruited Monocytes Promote, Allergic Lung Inflammation in Murine Models of Asthma. J Immunol. 2014; 193:4245–4253. [PubMed: 25225663]

71. Nimmagadda S, Pullambhatla M, Stone K, Green G, Bhujwalla ZM, Pomper MG. Molecular Imaging of Cxcr4 Receptor Expression in Human Cancer Xenografts with [64Cu]AMD3100 Positron Emission Tomography. Cancer Res. 2010; 70:3935–3944. [PubMed: 20460522]

72. Liu Y, Pressly ED, Abendschein DR, Hawker CJ, Woodard GE, Woodard PK, Welch MJ. Targeting Angiogenesis Using a C-Type Atrial Natriuretic Factor-Conjugated Nanoprobe and Pet. J Nucl Med. 2011; 52:1956–1963. [PubMed: 22049461]

73. Bonig H, Chudziak D, Priestley G, Papayannopoulou T. Insights into the Biology of Mobilized Hematopoietic Stem/Progenitor Cells through Innovative Treatment Schedules of the CXCR4 Antagonist AMD3100. Exp Hematol. 2009; 37:402–415. [PubMed: 19157683]
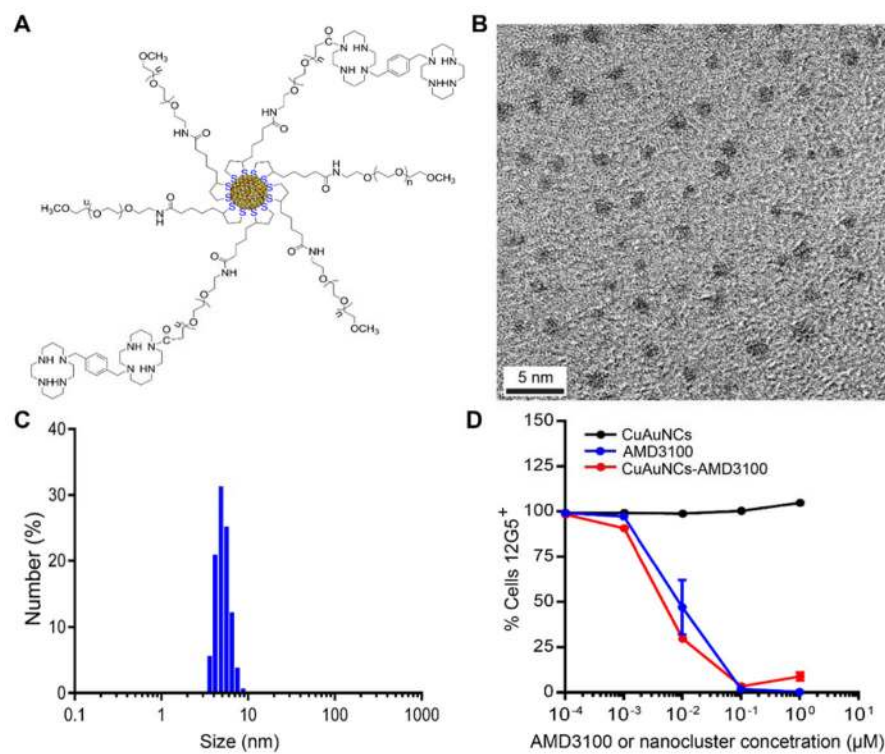
Figure 1.
Characterization of CuAuNCs-AMD3100 (A) Schematic of CuAuNCs-AMD3100 showing the molecular ratio of TA-PEG-OMe to TA-PEG-AMD3100 conjugated on the surface as 2:1. (B) TEM image and (C) dynamic light scattering histogram of CuAuNCs-AMD3100 showing uniformed size distribution. (D) *In vitro* binding affinity comparison of CuAuNCs, AMD3100 and CuAuNCs-AMD3100 in human G2 acute lymphoblastic leukemia (All) cells expressing CXCR4 receptors.
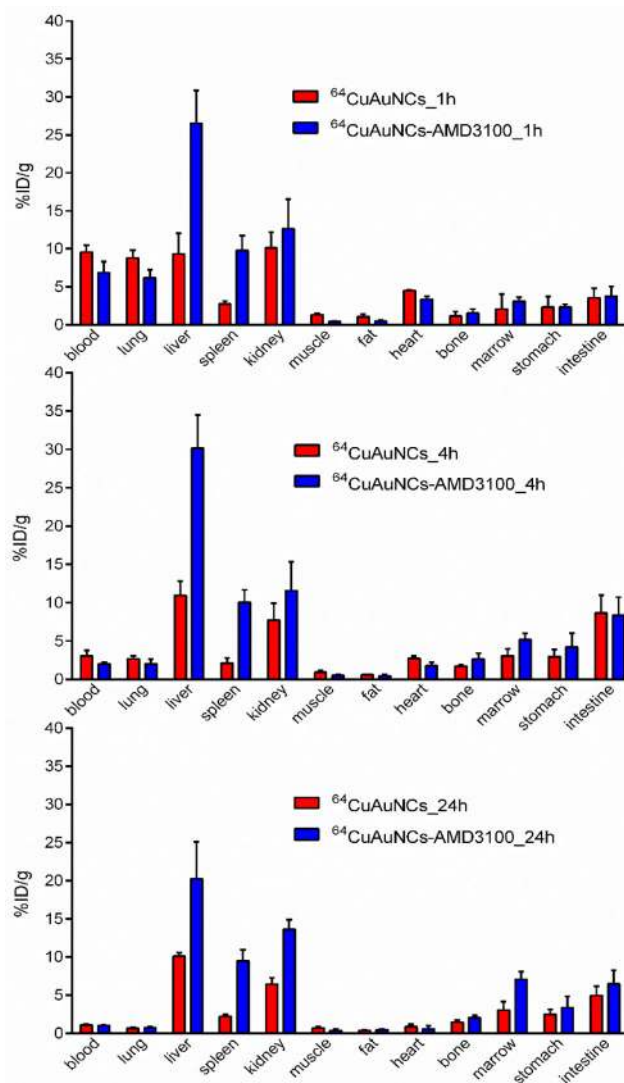
Figure 2.
Biodistribution of ^{64}CuAuNCs and ^{64}CuAuNCs-AMD3100 in wild type Balb/c mice at 1 h, 4 h, 24 h post intravenous injection *via* tail vein (370 kBq/100 µL injection, n=3/group).
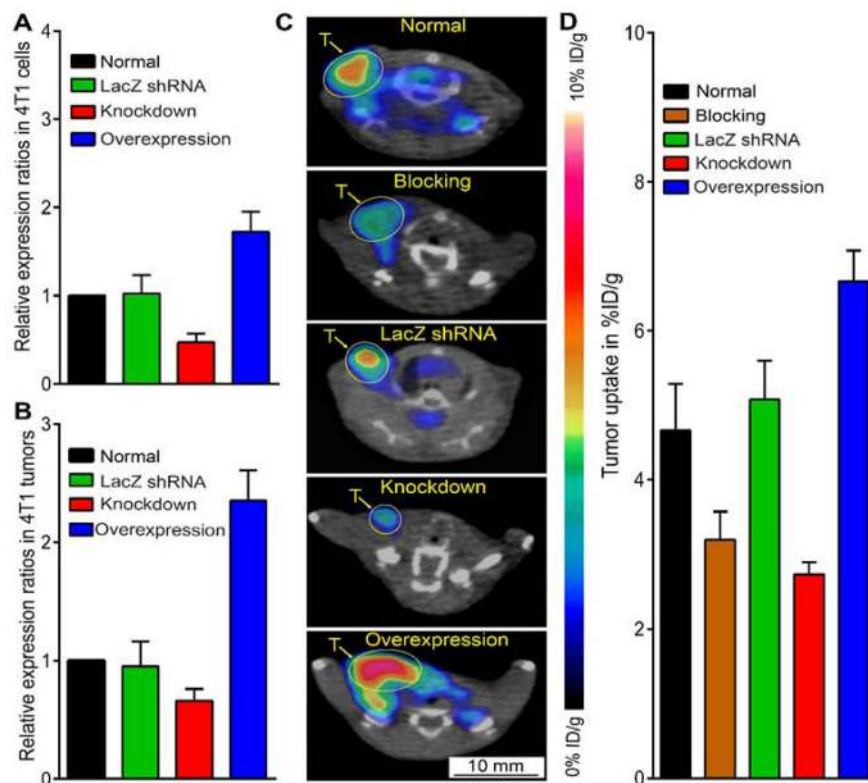
Figure 3.
Characterization of ^{64}CuAuNCs-AMD3100 imaging sensitivity in engineered 4T1 models expressing various levels of CXCR4. A) RT-PCR of CXCR4 in normal, LacZ shRNA, knockdown and overexpression 4T1 cells showing the different expression of receptor. B) RT-PCR of CXCR4 in engineered 4T1 tumors collected at 1 week post implant showing the variation of receptor levels *in vivo*, consistent with *in vitro* cell data. C) Representative transverse PET images demonstrating the specific detection of tumors in the engineered 4T1 tumors models. D) Quantitative tumor uptake of ^{64}CuAuNCs-AMD3100 in 4T1 models showing the sensitivity detecting various CXCR4 levels. T: tumor. CT scale bar on representative PET/CT image was the same for all images.
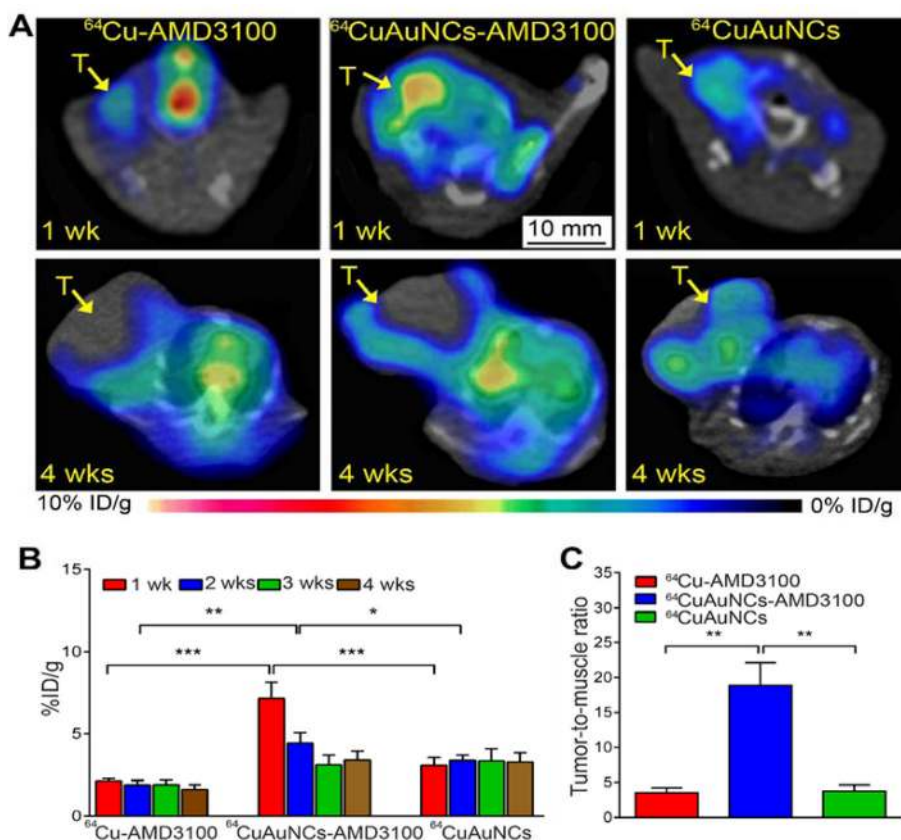
Figure 4.
A) Representative PET/CT transverse images of ^{64}Cu-AMD3100, [64]CuAuNCs-AMD3100 and [64]CuAuNCs showing the tracer accumulation in the same tumors of 4T1 model at 1 week and 4 weeks post tumor implant. ^{64}Cu-AMD3100 images were acquired by 0–60 min dynamic scan due to the fast pharmacokinetics. The targeted [64]CuAuNCs-AMD3100 and non-targeted [64]CuAuNCs PET images were acquired by 1 h static scan at 24 h post injection. B) Quantitative tumor uptake (%ID/g) of the three radiotracers in 4T1 tumor model at 1, 2, 3 and 4 weeks post tumor implant. C) tumor-to-muscle uptake ratios of the three radiotracers in 4T1 tumor model at 1 week post tumor implant. * $p < 0.05$, ** $p < 0.005$, *** $p < 0.001$. T: tumor. CT scale bar on representative PET/CT image was the same for all images.
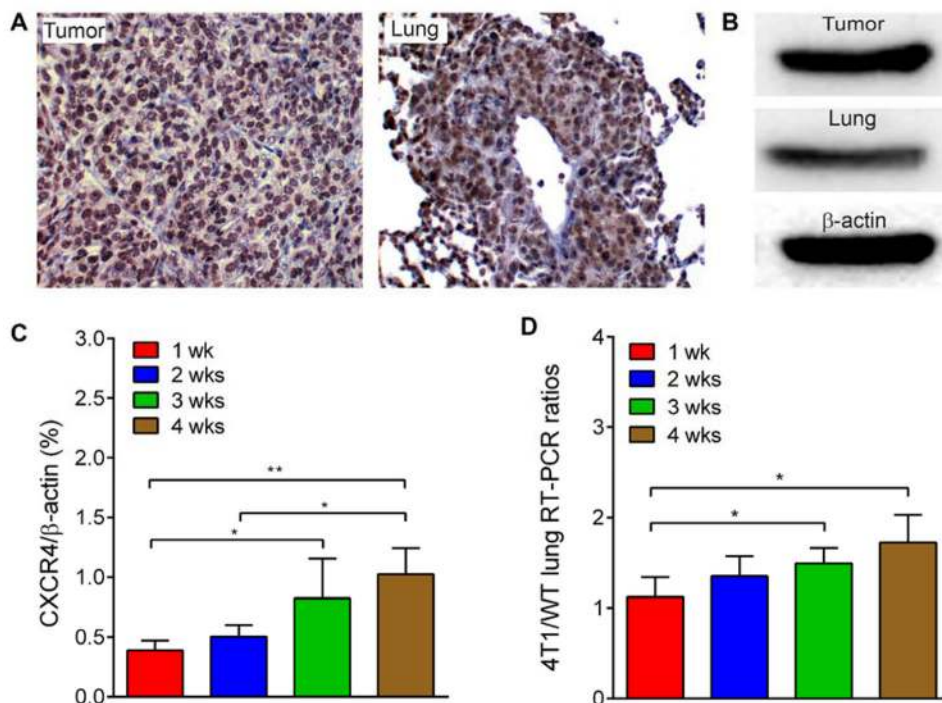
Figure 5.
(A) DAB (3,3′-diaminobenzidine) immunohistochemical staining of CXCR4 (brown) in 4T1 tumor at 1 week post implant and metastatic lung at 4 weeks post tumor implant showing the dense expression of the receptor in tumor cells. (B) Western blot of tumor at 1 week post implant and metastatic lung at 4 weeks post tumor implant showing the presence of the protein in the 4T1 model (C) RT-PCR of CXCR4 in tumor during the 4 weeks showing increased expression with the progression of model. (D) CXCR4 RT-PCR ratio between the lungs of tumor bearing mice and wild-type (WT) mice showing elevated expression of CXCR4 during the progression of model. All panels are 20×. * $p < 0.05$, ** $p < 0.005$, *** $p < 0.001$.
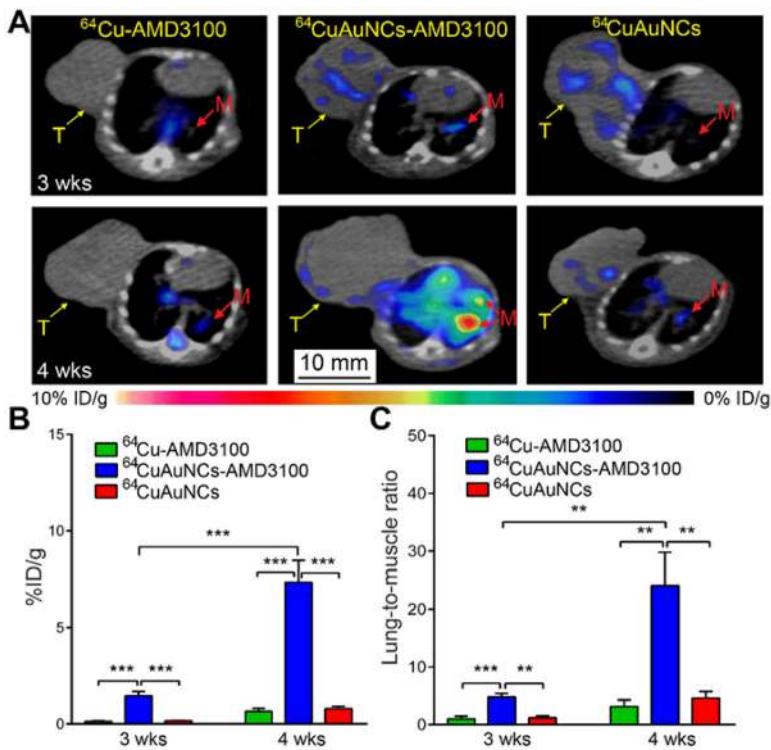
Figure 6.
A) Representative PET/CT transverse images of ^{64}Cu-AMD3100, [64]CuAuNCs-AMD3100 and [64]CuAuNCs showing the tracer accumulation in the lung of same 4T1 tumor bearing mice at 3 and 4 weeks post tumor implant. ^{64}Cu-AMD3100 images were acquired by 0–60 min dynamic scan due to the fast pharmacokinetics. The targeted [64]CuAuNCs-AMD3100 and non-targeted [64]CuAuNCs PET images were acquired by 1 h static scan at 24 h post injection. B) Quantitative lung metastasis uptake and C) lung-to-muscle uptake ratios of the three radiotracers in the lungs of same 4T1 tumor bearing mice at 3 weeks and 4 weeks post tumor implant. * $p < 0.05$, ** $p < 0.005$, *** $p < 0.001$. T: tumor. M: metastasis. CT scale bar on representative PET/CT image was the same for all images.